Cordula Braun*, Liuda Mereacre and Helmut Ehrenberg

$PbCN_2$ – an elucidation of its modifications and morphologies

https://doi.org/10.1515/znb-2021-0141
Received September 20, 2021; accepted October 8, 2021;
published online November 1, 2021

Abstract: Concerning the crystal structure of $PbCN_2$ there exist two different descriptions in the literature, one based on the non-centrosymmetric structure, space group $Pna2_1$, another one on the centrosymmetric one in space group *Pnma*. To elucidate the conditions for their appearance, comprehensive preparative and structural investigations have been conducted which proved the existence of two distinct modifications of $PbCN_2$. A detailed comparison of the two phases is provided. The growth conditions and crystallization processes of the two $PbCN_2$ structures are reported with focus on the influence of the pH value on the products. Depending on the growth conditions several different morphologies arise, namely $PbCN_2$ in needle-shaped and platelet-shaped crystals, as well as pompon-shaped and lance-shaped crystals.

Keywords: carbodiimide; cyanamide; lead; morphology; synthesis conditions.

Dedicated to Professor Richard Dronskowski on the Occasion of his 60th Birthday

1 Introduction

Cyanamides and carbodiimides constitute a fundamental class of compounds in the field of solid-state chemistry, which have gained increased attention within the past decade as remarkably high thermal and chemical resistances were discovered, which make them excellent candidates for many applications.

In the general formula $M_x(NCN)_y$ (M = alkali, alkaline Earth, main group, transition or rare Earth metals) the $(NCN)^{2-}$ ions can appear with the symmetric carbodiimide ($[N{=}C{=}N]^{2-}$) or the unsymmetric cyanamide ($[N{\equiv}C{-}N]^{2-}$) form depending on the nature of the metal cations [1–42]. Doped with divalent as well as trivalent rare Earth elements, metal cyanamides and carbodiimides emerged as excellent candidates for luminescent host materials [24, 28, 29, 35, 43–52].

The application of main group and transition metal carbodiimides MCN_2 (M = Cu, Zn, Mn, Fe, Co, Ni and Pb, Sn) as negative electrode materials for lithium and sodium ion batteries proved them to exhibit very good cycling properties [13, 24, 35, 38, 53–55].

Mott–Schottky experiments revealed that carbodiimides could be *n*-type semiconductors with a flat-band potential, and therefore the position of the valence band edge could be suitable for photochemical water oxidation [32].

Two routes are commonly used for synthesizing cyanamides and carbodiimides. In early protocols they were prepared by a reaction between an aqueous solution of a cyanamide with the corresponding metal acetate. The addition of an ammonia solution led to the formation of a precipitate, which was then filtered, washed and dried.

Another approach for synthesis emerged with the solid-state metathesis (SSM) using Na_2CN_2 with the respective metal chlorides or halides [34, 56–59]. Solid-state metathesis reactions do not require high temperatures. By utilizing the intrinsic energy of the reactants to promote an exchange of ions under relatively mild conditions, the desired reaction product and a co-produced salt are obtained. Note that Cooper [1] realised the synthesis of $PbCN_2$ with an exchange of ions within the melt of the co-produced salt.

It is thus essential to elucidate the building mechanisms of the structures in order to better understand and tune the properties of the products and explore their application capabilities in materials science.

In 1964 Cooper et al. [1] reported the structures of some inorganic cyanamides, including the structure of a $PbCN_2$ sample which crystallized in the non-centrosymmetric space group $Pna2_1$. In 2000 Liu and coworkers [2] presented a crystal structure refinement of lead a cyanamide $PbCN_2$ in the centric space group *Pnma* where they postulated: "*it became clear that a center of symmetry had been overlooked in the 1964 structure determination of PbNCN, carried out in space group* $Pna2_1$ [1]" and "*important structural details*

***Corresponding author: Dr. Cordula Braun**, Karlsruhe Institute of Technology (KIT), Institute for Applied Materials (IAM), Herrmann-von-Helmholtz-Platz 1, D-76344 Eggenstein-Leopoldshafen, Germany, E-mail: cordula.braun@kit.edu
Liuda Mereacre and Helmut Ehrenberg, Karlsruhe Institute of Technology (KIT), Institute for Applied Materials (IAM), Herrmann-von-Helmholtz-Platz 1, D-76344 Eggenstein-Leopoldshafen, Germany

such as the angle and C-N bond lengths were of limited accuracy" [2].

Cooper [1] as well as Liu [2] described the $PbCN_2$ crystals as yellow needles. However, Cooper mentioned also that "*the needles form as thin plates perpendicular to the b axis*" [1]. Möller et al. [60] investigated the high-pressure behaviour of $PbCN_2$ in 2018. Notably, in the methods section it is stated that a pH value of 10 is needed for the synthesis while in the original work of Liu [2] "only a few drops of ammonia solution" [2] are mentioned and no more detailed information is given.

A recent paper of Qiao et al. [59] presented a new synthesis route via solid-state metathesis (SSM) for $PbCN_2$. Scanning electron micrographs revealed that the so obtained $PbCN_2$ crystals have the shape of a flowers petal. Astonishingly, the authors did not discuss why here a different crystal shape instead of the known needle shape [2] was found and how the morphology of the compound is affected by the different synthesis routes.

Therefore it appeared to be worth having a closer look at the crystal morphologies and the crystal growth conditions of $PbCN_2$ and to elucidate the circumstances of the formation of its distinct structures [1, 2].

2 Results and discussion

2.1 Synthesis

To elucidate whether there may be two different modifications of $PbCN_2$, the compound was prepared according to the given synthesis routes in the respective reports [1, 2]. One way is synthesizing $PbCN_2$ via lead acetate and sodium cyanamide [1] (see Eq. 1).

The other route is the synthesis using lead acetate and hydrogen cyanamide [2] according Eq. (2).

Acetate/salt route:

$$Pb(CH_3COO)_2 + Na_2CN_2 \rightarrow PbCN_2 + 2CH_3COONa \quad (1)$$

Acetate/acid route:

$$Pb(CH_3COO)_2 + H_2CN_2 + 2NH_3 \rightarrow PbCN_2 + 2CH_3COONH_4 \quad (2)$$

The powder X-ray diffraction patterns of the products seem to match with the corresponding reference patterns from the literature [1, 2].

In Figure 1 a powder pattern is depicted, which shows two reflections very close to each other, where only one would be expected, and reflects a coexistence of two very similar phases with slightly different lattice parameters. This sample was obtained from centrosymmetric $PbCN_2$ [2], which has been heated up in NH_3 atmosphere to 200 °C for 18 h and then to 250 °C for 50 h. The powder pattern was recorded *ex situ* at room temperature on a STOE STADI P powder diffractometer in Debye-Scherrer geometry with Ge (111)-monochromatized Cu$K\alpha_1$ radiation (λ = 1.54060 Å). The observed and calculated powder X-ray diffraction patterns as well as their difference curves after Rietveld refinement [61] are shown in Figure 1 for a two-phase model based on the previously reported centrosymmetric [2] and non-centrosymmetric [1] structure models. Note that the smaller unit cell is assigned to the centrosymmetric structure model, because this is expected to be the high-temperature phase in comparison with the non-centrosymmetric phase. The intensities for the powder patterns of the centrosymmetric and non-centrosymmetric structures are very similar and do not allow an unambiguous assignment. Crystallographic data and details of the Rietveld refinement are listed in Table 1.

The appearance of the coexistence of two phases after the high-temperature treatment raises questions regarding the stability ranges of both phases. Therefore, centrosymmetric $PbCN_2$ was heated up with holding times of 5 h at temperatures of 150, 175, 200, 300, 400 and 500 °C in NH_3 atmosphere. XRD powder patterns were recorded *ex situ* after cooling back to RT. Two sections of the diffraction patterns are shown in Figure 2. The first one from 2θ = 23°–25° corresponds to the 011 reflections, the range from 28° to 30° to the 111 reflections of both structure models.

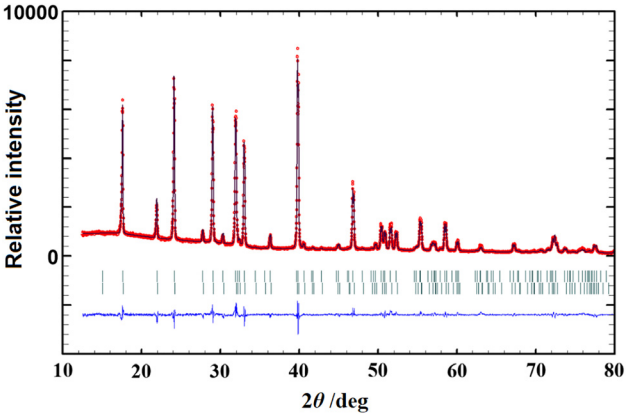

Figure 1: Observed (red circles) and calculated (black line) powder X-ray diffraction pattern of $PbCN_2$ [2] (after thermal treatment at 200 °C for 18 h and at 250 °C for 50 h in NH_3 atmosphere) showing a coexistence of both $PbCN_2$ modifications. The blue curve is the difference between observed and calculated patterns after Rietveld refinement (λ = 1.54060 Å). The positions of the Bragg reflections are shown by green bars, the upper line belongs to the larger unit cell (assumed to represent the non-centrosymmetric structure), the lower line to the smaller unit cell (assumed to represent the centrosymmetric structure).

Table 1: Crystallographic data for $PbCN_2$ [1, 2] (estimated standard deviation in parentheses).

	Centrosymmetric structure [2]	Non-centrosymmetric structure [1]
Formula	$PbCN_2$	
Formula mass/ g mol^{-1}	158.71	
Crystal system	Orthorhombic	Orthorhombic
Space group	*Pnma* (no. 62)	$Pna2_1$ (no. 33)
Cell parameters		
a/Å	5.55458(6)	5.57088(6)
b/Å	3.86783(4)	11.7931(4)
c/Å	11.7535(3)	3.87923(4)
Phase fraction/%	54(1)	46(1)
Cell volume/Å^3	252.514(7)	254.858(9)
Formula units *Z*	4	4
Diffractometer	STOE STADI P	
Radiation; λ/Å	Cu$K\alpha_1$; 1.540598	
Monochromator	Ge 111 (curved)	
Temperature/K	293	
Data range in 2θ; step width/degree	12–80; 0.01	
Structure refinement	Rietveld refinement, FullProf [61]	
Background treatment	18 fixed background points	
Profile function	Pseudo-Voigt (FullProf no. 7)	
R_{Bragg}	4.26	4.74
GoF	1.5	
Reduced χ^2	2.13	

Note that atomic coordinates were taken from Refs. [1] and [2], respectively, and were not refined.

The reflections on the right side (higher diffraction angles) of the dark blue curve and the light blue curve are at the same position and, therefore, correspond to centrosymmetric $PbCN_2$ [2] at RT. For the 175 °C sample the reflections in the red pattern are shifted and are at the same position as the reflections on the left side (lower diffraction angles) of the dark blue curve and, therefore, assigned to non-centrosymmetric $PbCN_2$ [1]. If the sample was heated to 200 °C, the reflections shift back to the positions of centrosymmetric $PbCN_2$ [2]. This indicates that the centrosymmetric sample is metastable at room temperature. The temperature of 175 °C is sufficient to overcome activation barriers and enables a transformation into the thermodynamically stable non-centrosymmetric phase. The higher temperature of 200 °C is already in the stability range of the high-temperature centrosymmetric phase, which remains metastable at room temperature. If the sample was heated to 400 °C or higher, irreversible decomposition takes place as detected by additional reflections due to metallic Pb in the patterns.

Centrosymmetric $PbCN_2$ [2] was also analyzed by differential scanning calorimetry (DSC). Heating up the metastable centrosymmetric phase resulted in an exothermic transition at around 177 °C, which is assigned as the transformation into the non-centrosymmetric phase of $PbCN_2$ [1] which is thermodynamically stable at this temperature (see Figure 3). There is a second but much weaker exothermic effect visible around 210 °C, indicating the back transformation to centrosymmetric $PbCN_2$, which is the thermodynamically stable phase at such higher temperatures [2].

On the other hand, DSC measurements of non-centrosymmetric $PbCN_2$ [1] revealed a very much weaker exothermic transition at around 170 °C, which is probably due to a small amount of metastable centrosymmetric $PbCN_2$ in this sample. Again, the transformation into the high-temperature centrosymmetric phase is observed at around 210 °C.

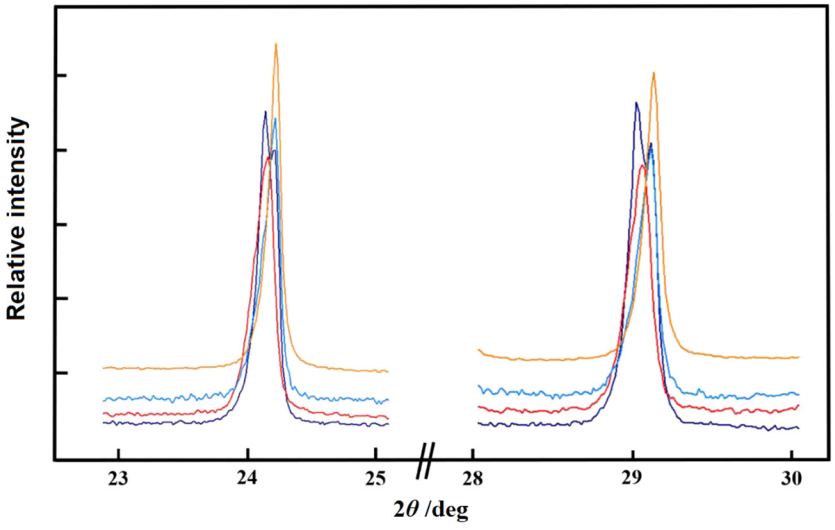

Figure 2: Enlargement of the reflections at 24° and 29° in 2θ of the initially centrosymmetric $PbCN_2$ [2] after different treatments. The light blue pattern is from the as prepared centrosymmetric sample at room temperature. The other patterns refer to samples at room temperature after interim heatings to 175 °C (red) or 200 °C (orange). The dark blue pattern is a section of Figure 1 with overlapping reflections and corresponds to the previously described sample.

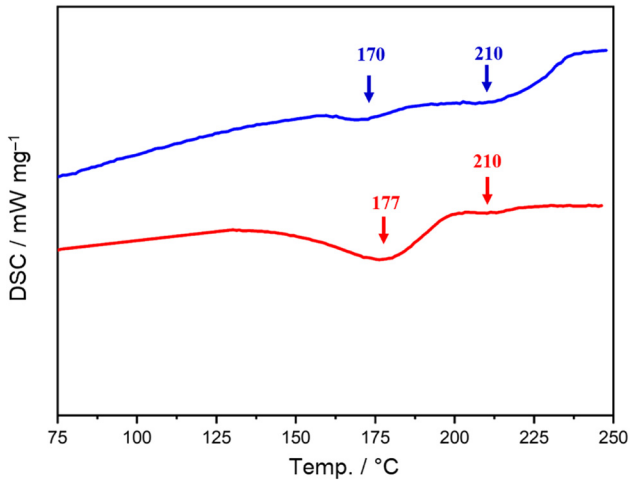

Figure 3: DSC measurements of non-centrosymmetric $PbCN_2$ [1] (blue) and centrosymmetric $PbCN_2$ [2] (red) up to 250 °C.

The partial transformation of the centrosymmetric phase into the non-centrosymmetric phase at 175 °C was also confirmed by *in situ* temperature dependent X-ray diffraction studies. Again, the metastability of the high-temperature centrosymmetric phase down to room temperature was confirmed. These experiments were performed on an initially centrosymmetric sample in a capillary, sealed under Ar atmosphere.

For the *in situ* temperature dependent powder X-ray diffractometry (TDXRD) measurements, centrosymmetric $PbCN_2$ [2] was heated up from RT to 300 °C with holding periods and equilibration at temperatures of 150, 175, 200 and 300 °C. Each temperature step was kept for 1 h.

At 175 °C we see the appearance of two distinct sets of reflections corresponding to non-centrosymmetric $PbCN_2$ [1] and centrosymmetric $PbCN_2$ [2]. The overlap of both sets of reflections confirms the coexistence of the two phases up to 200 °C. Afterwards, the temperature was reduced again and diffraction patterns were recorded at the same temperatures. The overlap of reflections persists down to RT.

2.2 Comparison of the two modifications of $PbCN_2$

The structures of non-centrosymmetric and centrosymmetric $PbCN_2$ [1, 2] are very similar and differ only very slightly in some interatomic distances and angles. A comprehensive description shall be waived as this has already been provided in several other references [1, 2, 59, 60, 62]. In the following these differences shall be illustrated by some detailed pictures.

The crystal structures of centrosymmetric $PbCN_2$ [2] (see Figures 4a and 5a) and non-centrosymmetric $PbCN_2$ [1] (see Figures 4b and 5b) viewed along the [001] and [010] direction, respectively, show alternating layers of Pb^{2+} atoms and $(N–C\equiv N)^{2-}$ groups like most other metal carbodiimides, e.g. $SnCN_2$ [24, 26, 35]. However, in $SnCN_2$ [24, 26, 35] the cross linking of these layers leads to a three-dimensional network.

The rhombs in non-centrosymmetric $PbCN_2$ [1] are more compressed than in centrosymmetric $PbCN_2$[2] resulting in an endocyclic angle of 93° [1] instead of 95° [2] and therefore the angles of the adjacent rhombs are smaller

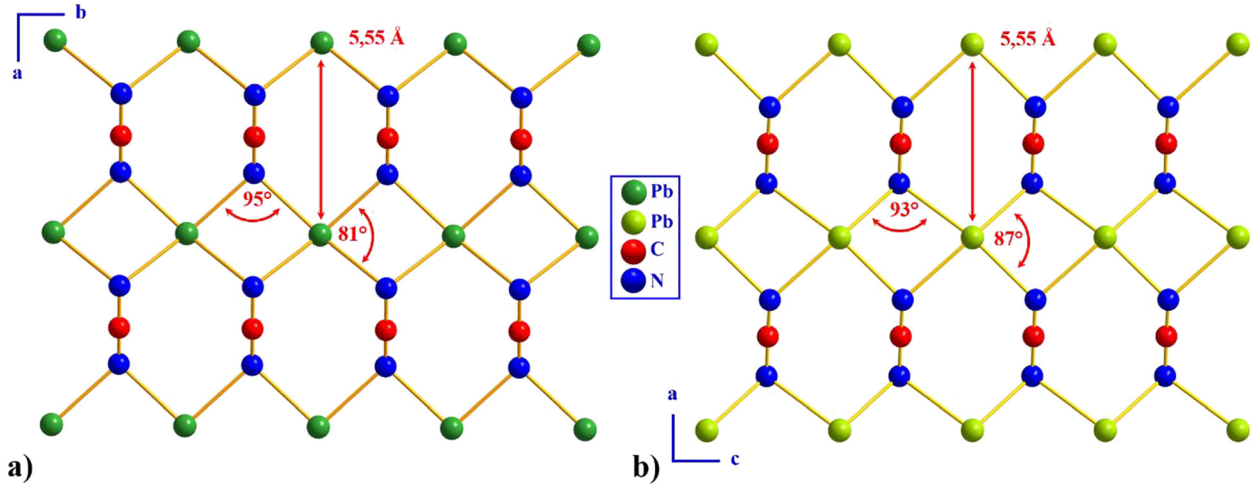

Figure 4: Comparison of (a) centrosymmetric $PbCN_2$ [2] viewed along [001] and (b) non-centrosymmetric $PbCN_2$ [1] viewed along [010] (Pb atoms in green [2] and light green [1], C atoms in red and N atoms in blue). Note that different cell settings are used to describe the two structures. Therefore, [001] and [010] refer topologically to the same directions.

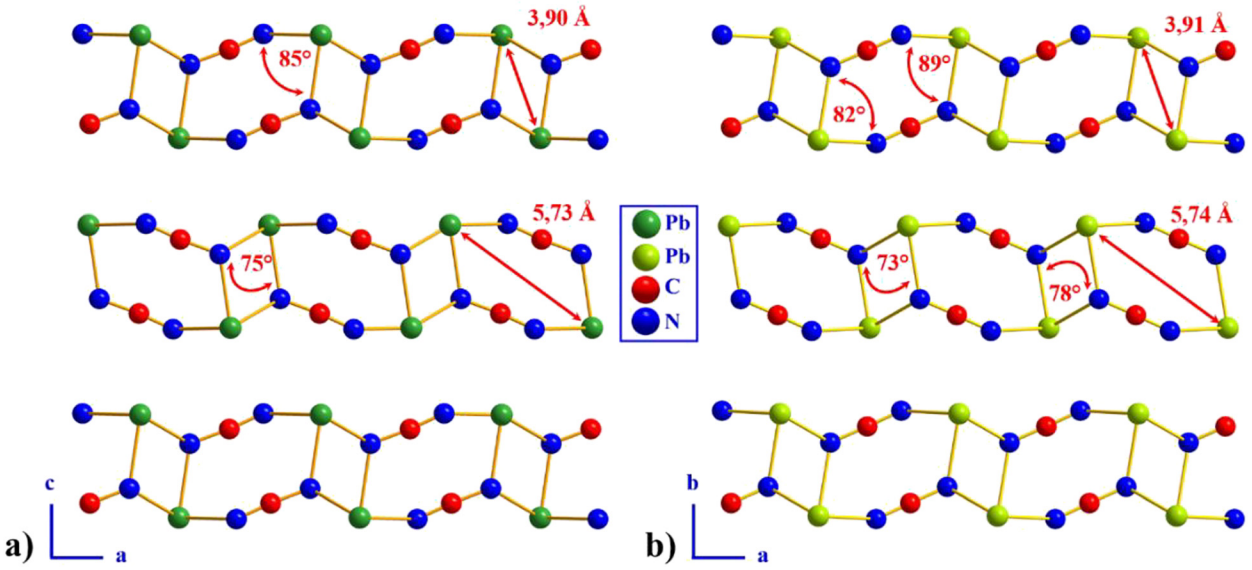

Figure 5: Comparison of (a) centrosymmetric $PbCN_2$ [2] viewed along [010] and (b) non-centrosymmetric $PbCN_2$ [1] viewed along [001] (Pb atoms in green [2] and light green [1], C atoms in red and N atoms in blue). Note that the *a* axes are topologically the same in both structure settings.

in centrosymmetric $PbCN_2$ [2] (81°) and bigger in non-centrosymmetric $PbCN_2$ [1] (87°) (see Figure 4).

Corrugated double layers can be found for centrosymmetric $PbCN_2$ [2] along [010] and for non-centrosymmetric $PbCN_2$ [1] along [001] (see Figure 5). The non-centrosymmetric polymorph [1] exhibits two slightly different endocyclic angles (within the rhombs) of 82° und 89° (see Figure 5b) while in the centrosymmetric phase [2] both angles are 85°. (see Figure 5a). The diagonals of the rhombs vary only marginally with 5.73 and 5.74 Å.

Figure 6 shows the non-centrosymmetric and centrosymmetric $PbCN_2$ phases [1, 2] viewed along [100]. Again,

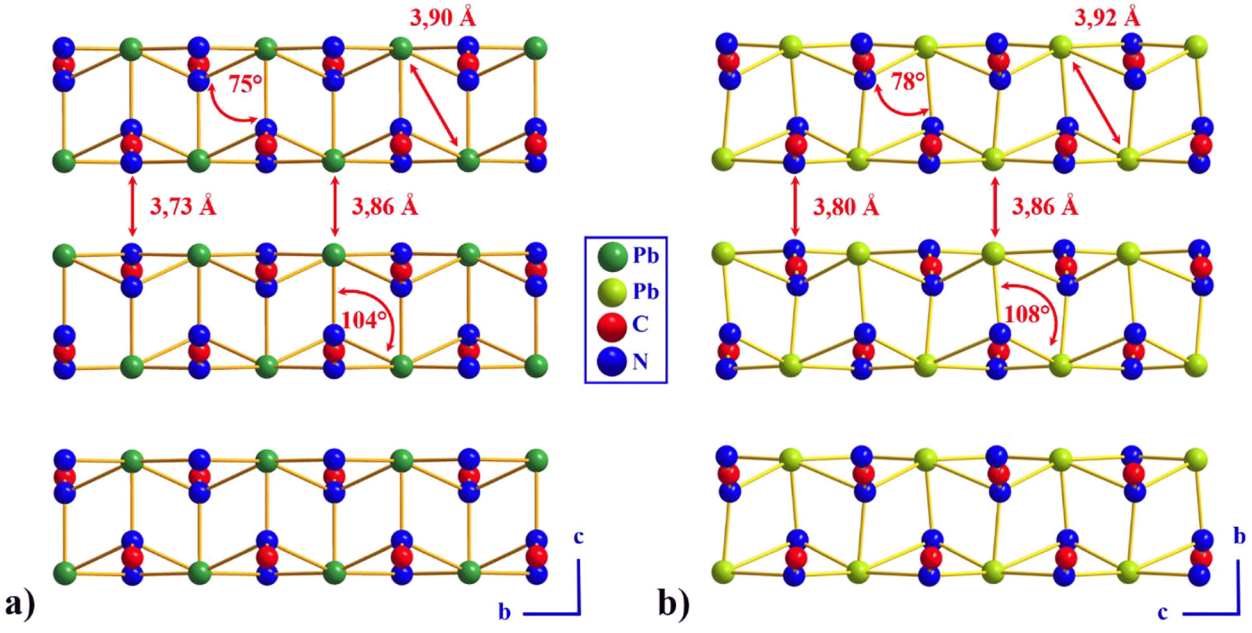

Figure 6: Comparison of (a) centrosymmetric $PbCN_2$ [2] viewed along [100] and (b) non-centrosymmetric $Pb(CN)_2$ [1] viewed along [100] (Pb atoms in green [2] and light green [1], C atoms in red and N atoms in blue). Note that the *a* axes are topologically the same in both structure settings.

only small differences between the two polymorphs concerning the angles and the diagonals of the rhombs are visible. Due to the distortion the distances between the layers are larger in the non-centrosymmetric phase [1] (Figure 7).

$PbCN_2$ [1, 2] exhibits a significant deviation from the symmetric carbodiimide form resulting in two C–N bonds differing significantly in length (values taken from refs. [1, 2]). Within the $(N–C\equiv N)^{2-}$ groups the N–C single bond is 1.15 Å and the N≡C triple bond is 1.29 Å [2]. The non-centrosymmetric phase [1] on the other hand has for the N–C single bond 1.16 Å and for the N≡C triple bond 1.25 Å. The N–C≡N angle is 175 Å for centrosymmetric $PbCN_2$ [2] and 178° for non-centrosymmetric $PbCN_2$ [1].

2.3 Morphologies of $PbCN_2$

As mentioned above there are two possibilities to synthesize $PbCN_2$. One way is synthesizing $PbCN_2$ via Pb acetate and sodium cyanamide [1] (see Eq. 1) and the other route is the synthesis using Pb acetate and cyanamide [2] according (Eq. 2, above).

Even if the two synthesis routes look very similar at first glance, the reaction conditions differ significantly. The pH value during the synthesis and the timescale of the crystal growth turned out to be both relevant.

Cooper [62] described in his paper that the process according to Eq. (1) has to be a very slow ion diffusion and the mode of mixing of the two solutions is crucial. He also mentions that very long reactions and crystallization times of up to 36 h are essential. This is in agreement with our observations. One important difference to the synthesis route according to Eq. (2) is the pH level of 7–8.

Cooper [1] describes in his paper crystals in needle and platelet shape. At first look with a microscope this observation is completely correct (see Figure 8a). However, a very close look with SEM reveals that the needle formations consist of thin platelets as well (Figure 8b–d).

When choosing the synthesis route according to (Eq. 2), it is very important to layer the two solutions very slowly by adding the H_2CN_2/NH_3 solution dropwise to the solution of $Pb(CH_3COO)_2$. The reaction occurs at the interface and the precipitate acts then as a semipermeable membrane leading to a visible diffusion line and a subsequent diffusion area (Figure 9).

A fast mixing immediately results in crystallization of a yellow precipitate and the crystals are too small to identify any morphology. Note that also the time factor and holding periods have a significant influence.

To adjust the pH value, aqueous ammonia is added to the H_2CN_2 solution. As long as the solution is very acidic, there is no precipitation of $PbCN_2$. Depending on the pH value, different $PbCN_2$ morphologies are formed. The exact control of the pH value of the H_2CN_2/NH_3 solution is very important. The addition of a few drops of an ammonia solution, as it is described in ref. [2], is not detailed enough to control the crystallization process and to regulate which polymorph and morphology are formed.

At pH < 9 no crystals occur, and the crystallization starts at pH > 9 with the formation of very tiny needles of $PbCN_2$. At pH 9.9 (Figure 10d) a diffusion line is well visible in the middle of the interface, where the formation of very fine needles can be seen. Above this diffusion line conglomerates of fine needles are built (see Figure 10d, a and b), while below a small area where the needles change into a platelet shape (see Figure 10d, f) can be observed and then the formation of $PbCN_2$ in pompon-shaped crystals is preferred

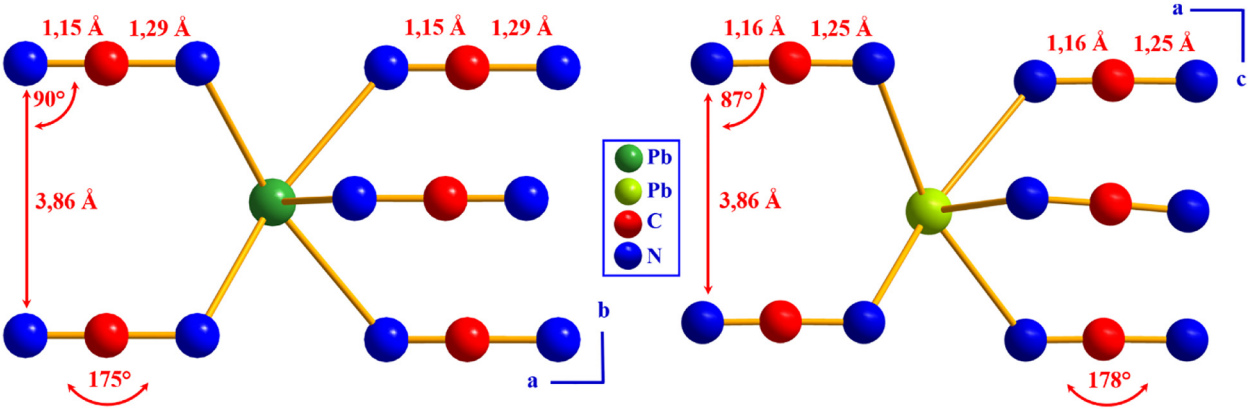

Figure 7: Comparison of the coordination sphere of the Pb atoms with bond lengths and angles in (a) centrosymmetric $PbCN_2$ [2] and (b) non-centrosymmetric $PbCN_2$ [1] (Pb atoms in green [2] and light green [1], C atoms in red and N atoms in blue).

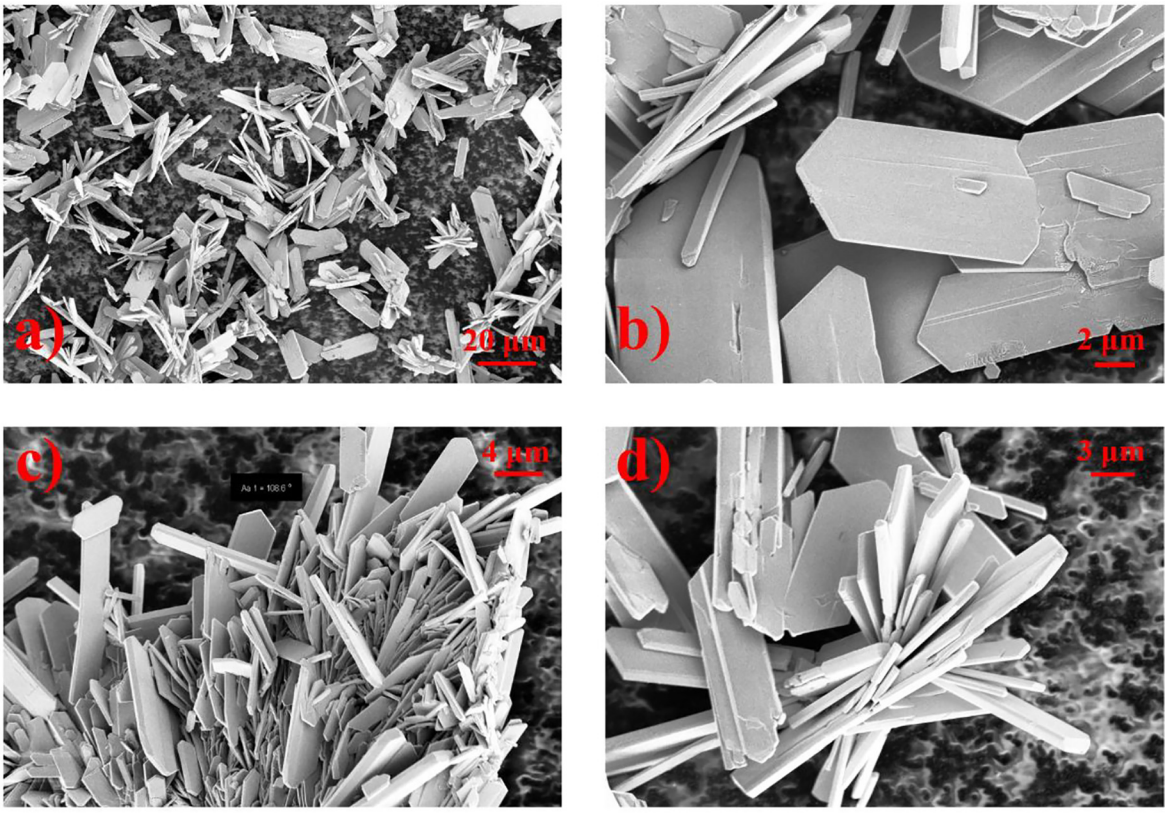

Figure 8: SEM pictures of platelet-shaped $PbCN_2$ obtained via the synthesis route of Cooper et al. [1].

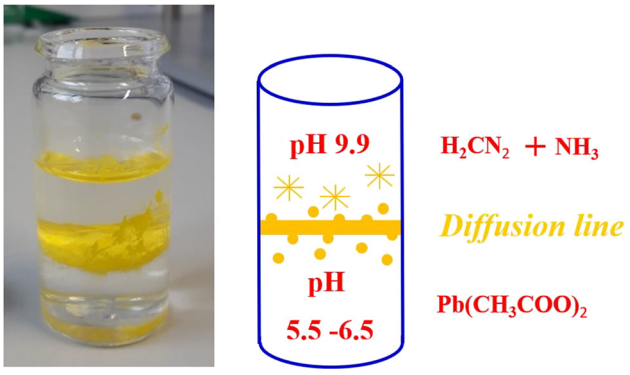

Figure 9: Reaction of lead acetate with cyanamide/ammonia at the interface of the solutions to produce $PbCN_2$.

(see Figure 10d, c). It appears that a very fine gradation of the pH value changes the morphology significantly.

Changing the pH value to level 11 a different appearance becomes visible. The diffusion line is still very clear but SEM pictures reveal that the needle shape of the crystals has changed into a lance-shaped form (Figures 10e and 14).

To sum up, the following morphologies can be observed: needle-shaped crystals (Figures 10a, b and 11), platelet-shaped crystals (Figures 10f and 12), pompon-shaped crystals (Figures 10c, 13) and lance-shaped $PbCN_2$ (Figures 10e and 14). In Figure 11b, c and d as well as in Figures 12d and 13b it is clearly visible that the needles/platelets/pompons have a twofold rotation axis and a mirror plane (Figure 14).

3 Conclusions

With these investigations we could prove the existence of two modifications of $PbCN_2$ [1, 2] Liu et al. [2] as well as Cooper [1] reported crystallographically correct structures of $PbCN_2$, but for different modifications. The centrosymmetric form of $PbCN_2$ [2] is the high temperature phase which remains metastable at RT, and the non-centrosymmetric form [1] is the low temperature phase. Non-centrosymmetric $PbCN_2$ [1] can be synthesized at RT according to [1]. The non-centrosymmetric form of $PbCN_2$ [1] is present in a very small temperature window between 170° and around 200 °C reached upon heating of the centrosymmetric form. This is the temperature interval between sufficient thermal activation to promote the phase transition into the non-centrosymmetric

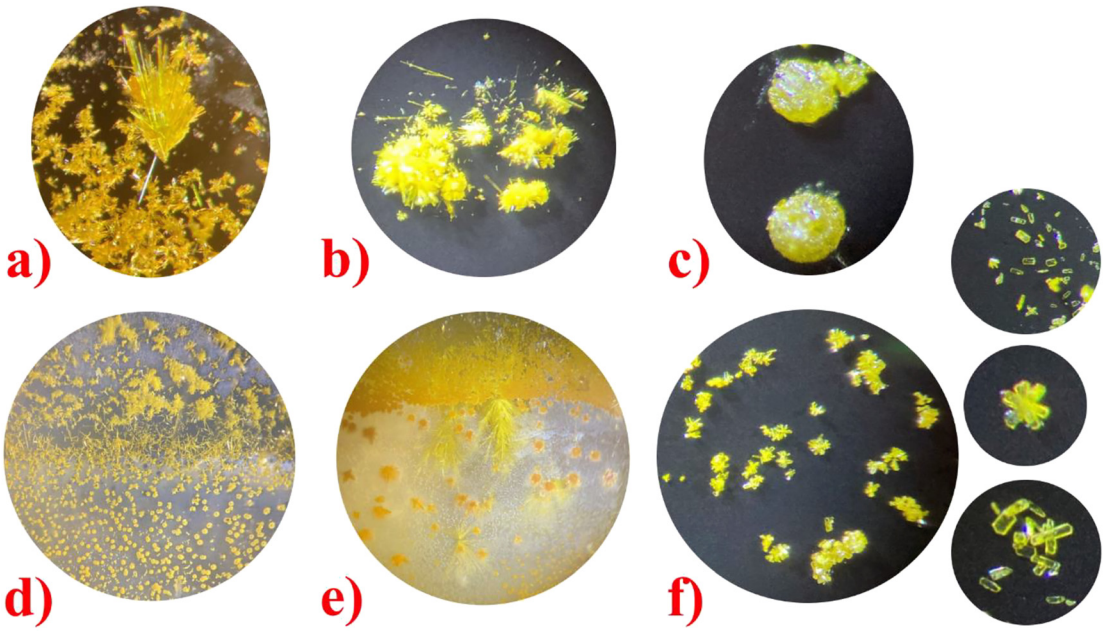

Figure 10: Different morphologies of $PbCN_2$ crystals: (a) and (b) $PbCN_2$ in needle shape, (c) $PbCN_2$ in pompon shape, (d) product of the synthesis at pH 9.9, and (e) at pH 11, (f) $PbCN_2$ in platelet shape.

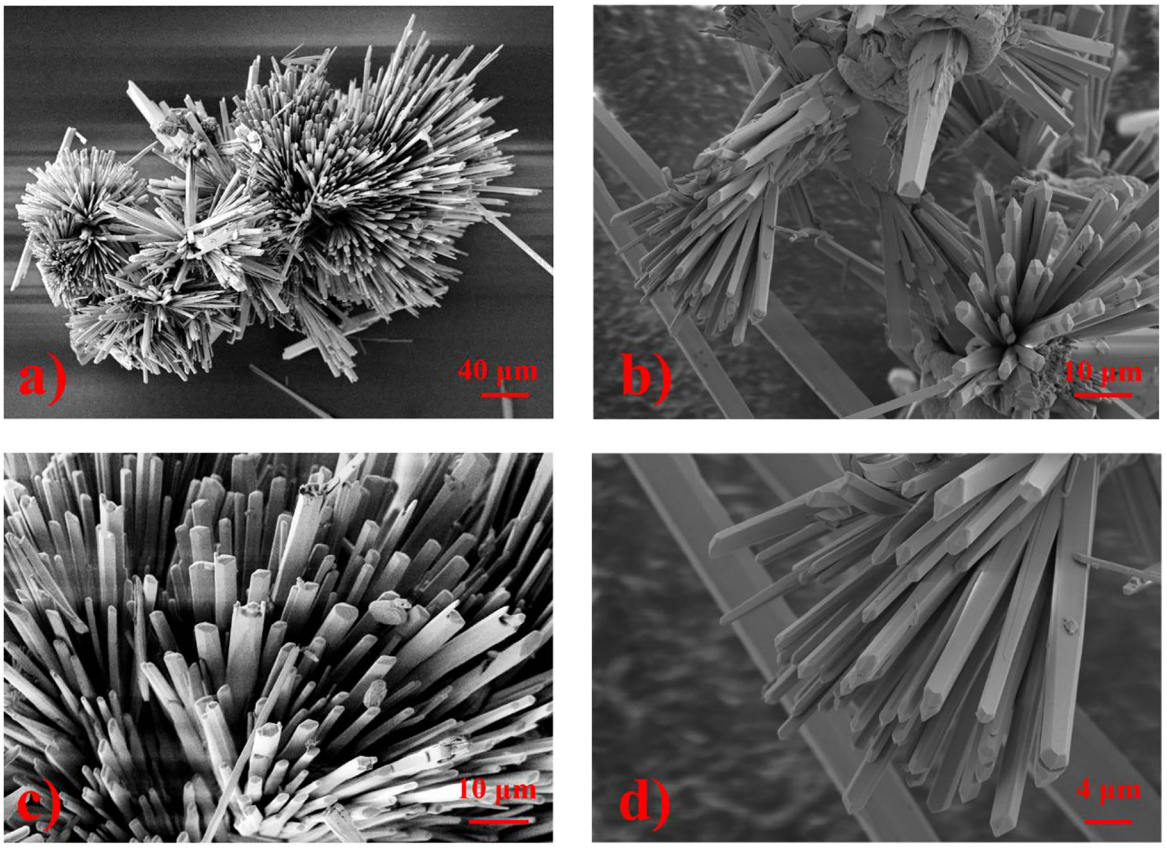

Figure 11: REM pictures of $PbCN_2$ in needle shape crystals.

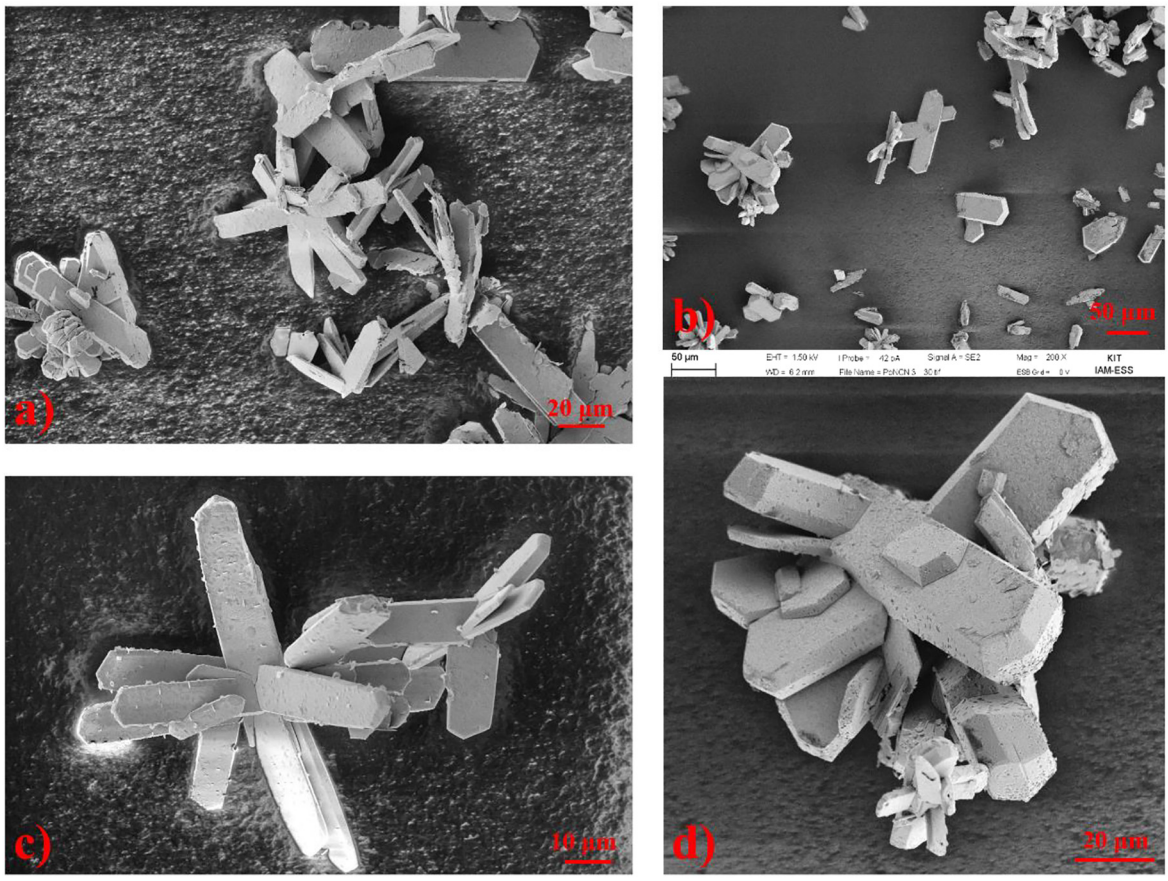

Figure 12: REM pictures of $PbCN_2$ in platelet shape crystals.

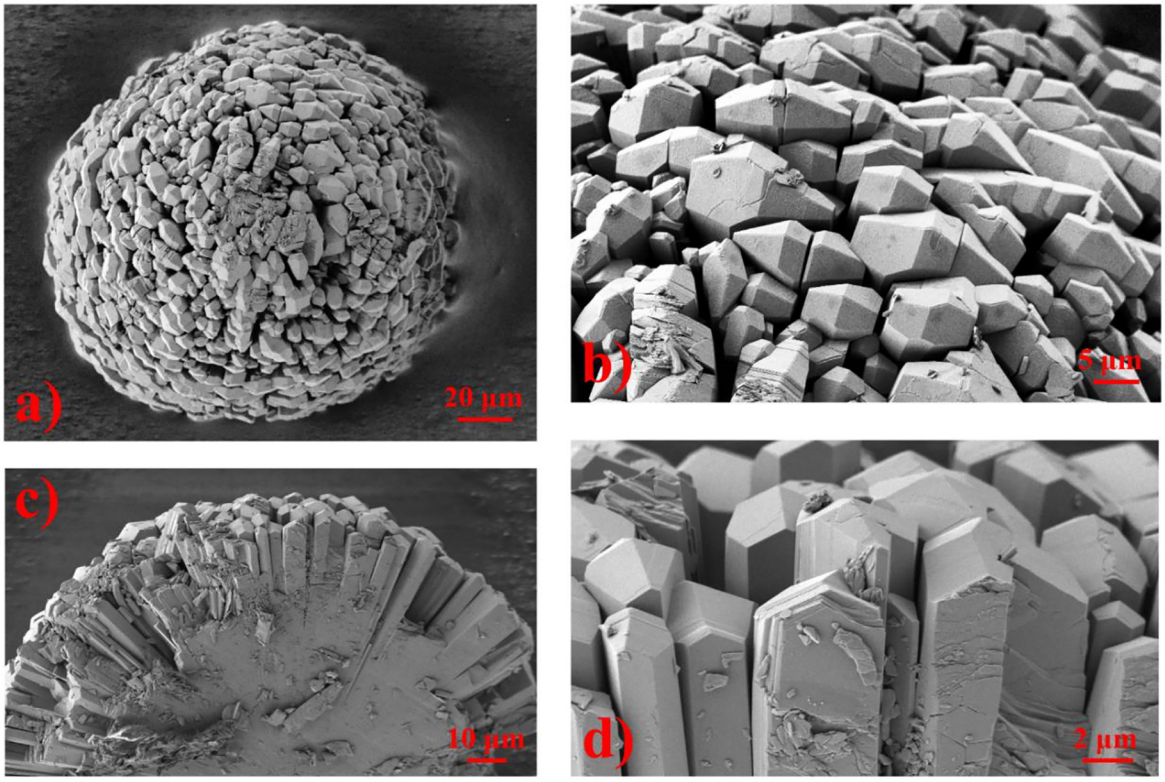

Figure 13: SEM pictures of $PbCN_2$ in pompon-shaped crystals.

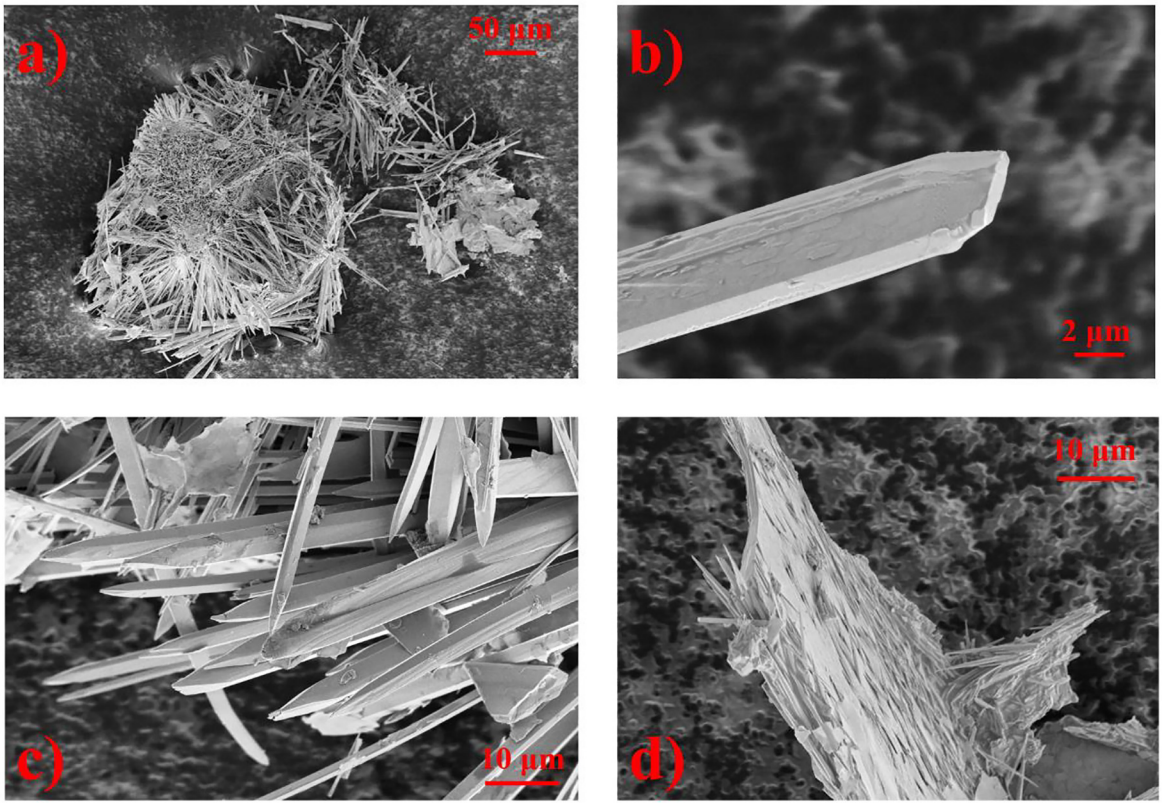

Figure 14: SEM pictures of lance-shaped crystals of $PbCN_2$.

low-temperature form and its upper stability limit before the transition into the centrosymmetric high-temperature phase.

High-temperature *in situ* investigations confirmed this observation, but proved as well that the non-centrosymmetric form of $PbCN_2$ [1] remains stable *in situ* upon cooling down to RT, while the centrosymmetric form of $PbCN_2$ is transformed only partially into the non-centrosymmetric form. Therefore, a two phase mixture is observed at RT where the thermodynamically stable room-temperature non-centrosymmetric phase coexists with the metastable centrosymmetric phase.

Analyzing non-centrosymmetric $PbCN_2$ [2] with differential scanning calorimetry (DSC) revealed a very small amount of the centrosymmetric modification in the sample by a weak exothermic signal [1] which disappeared upon the transformation into the high-temperature centrosymmetric phase at around 210 °C.

$PbCN_2$ is a very good example how details, either in the pH value, the growth conditions or in the crystallization processes can affect the resulting crystal structure. In the present case the pH value of the reaction medium plays an important role and influences the growth of several different morphologies, namely $PbCN_2$ in needle-shaped, in platelet-shaped, in pompon-shaped and lance-shaped crystals. This variety of crystal morphologies and its consequences for the materials properties of $PbCN_2$ have to be studied in further investigations.

4 Experimental section

4.1 Synthesis of $PbCN_2$

The syntheses of $PbCN_2$ were performed according the corresponding literature of Cooper [1] and Liu et al. [2].

4.2 X-ray diffraction

4.2.1 Powder diffraction: X-ray diffraction experiments on powder samples of $PbCN_2$ were performed on a STOE STADI P powder diffractometer in transmission geometry with Ge(111)-monochromatized Cu$K\alpha_1$ radiation (λ = 1.54060 Å). The sample was sealed between Kapton foils. A Rietveld refinement has been carried out using the program package FullProf [61]. Estimated standard deviations are calculated in agreement with Bérar and Lelann [63].

4.2.2 Temperature-dependent X-ray diffraction: The sample was measured on a STOE Fixed Stage diffractometer (λ = 0.709026 Å, Mo$K\alpha_1$ radiation, Ge(111)-monochromator) with an image-plate

detector (90°). This diffractometer is equipped with a graphite-rod furnace for sample heating.

4.3 EDX measurements

SEM was performed on a Zeiss Merlin microscope and for EDX we used a Quantax 400 system from Bruker.

4.4 DSC measurements

Differential scanning calorimetry (DSC) measurements were operated under an Ar atmosphere (Netzsch DSC 204F1 Phoenix) with combined FTIR gas analysis using a temperature scan rate of 5 K min^{-1}.

Acknowledgement: The authors gratefully acknowledge Udo Geckle (IAM-ESS KIT Karlsruhe) for the SEM measurements and Fa. Netzsch for fruitful discussions.
Author contributions: All the authors have accepted responsibility for the entire content of this submitted manuscript and approved submission.
Research funding: None declared.
Conflict of interest statement: The authors declare no conflicts of interest regarding this article.

References

1. Cooper M. J. *Acta Crystallogr*. 1964, *17*, 1452–1456.
2. Liu X., Decker A., Schmitz D., Dronskowski R. *Z. Anorg. Allg. Chem*. 2000, *626*, 103–105.
3. Down M. G., Haley M. J., Hubberstey P., Pulham R. J., Thunder A. E. *J. Chem. Soc. Chem. Commun*. 1978, *2*, 52–53.
4. Berger U., Schnick W. *J. Alloys Compd*. 1994, *206*, 179–184.
5. Liu X., Müller P., Kroll P., Dronskowski R. *Inorg. Chem*. 2002, *41*, 4259–4265.
6. Becker M., Nuss J., Jansen M. *Z. Naturforsch*. 2000, *55b*, 383–385.
7. Becker M., Jansen M. *Z. Anorg. Allg. Chem*. 2000, *626*, 1639–1641.
8. Becker M., Jansen M. *Acta Crystallogr*. 2001, *C57*, 347–348.
9. Stork L., Liu X., Fokwa B. P. T., Dronskowski R. *Z. Anorg. Allg. Chem*. 2007, *633*, 1339–1342.
10. Becker M., Nuss J., Jansen M. *Solid State Sci*. 2000, *2*, 711–715.
11. Tang X., Xiang H., Liu X., Speldrich M., Dronskowski R. *Angew. Chem*. 2010, *122*, 4846–4850.
12. Tang X., Xiang H., Liu X., Speldrich M., Dronskowski R. *Angew. Chem. Int. Ed*. 2010, *49*, 4738–4742.
13. Sougrati M. T., Darwiche A., Monconduit L., Stievano L., Hermann R. P., Mahmoud A., Herlitschke M., Dronskowski R., Liu X. *Metal Carbodiimides and Metal Cyanaymides as Electrode Materials*, 2015.
14. Baldinozzi G., Malinowska B., Rakib M., Durand G. *J. Mater. Chem*. 2002, *12*, 268–272.
15. Launay M., Dronskowski R. *Z. Naturforsch*. 2005, *60b*, 437–448.
16. Liu X., Krott M., Müller P., Hu C., Lueken H., Dronskowski R. *Inorg. Chem*. 2005, *44*, 4493001–4493003.
17. Boyko T. D., Green R. J., Dronskowski R., Moewes A. *J. Phys. Chem. C* 2013, *117*, 12754–12761.
18. Liu X., Wankeu M. A., Lueken H., Dronskowski R. *Z. Naturforsch*. 2005, *60b*, 593–596.
19. Liu X., Dronskowski R., Glaum R., Tchougréeff A. L. *Z. Anorg. Allg. Chem*. 2010, *636*, 343–348.
20. Krupinski K. *Molekulare Silylcarbodiimide-Synthese, Struktur und Reaktivität*. Dissertation, Technische Universität Bergakademie Freiberg, Freiberg (SA), 2012.
21. Liu X., Dronskowski R., Kremer R. K., Ahrens M., Lee C., Whangbo M.-H. *J. Phys. Chem. C* 2008, *112*, 11013–11017.
22. Corkett A. J., Chen Z., Bogdanovski D., Slabon A., Dronskowski R. *Inorg. Chem*. 2019, *58*, 6467–6473.
23. Dolabdjian K., Görne A. L., Dronskowski R., Ströbele M., Meyer H.-J. *Dalton Trans*. 2018, *47*, 13378–13383.
24. Braun C. *Doped Tin Carbodiimide and Use Thereof in Energy Storage Systems and as Phosphors*, 2019 EP19193824.0.
25. Filby A. G., Howie R. A., Moser W. *Dalton Trans*. 1978, 1797–1799. https://doi.org/10.1039/dt9780001797.
26. Löber M., Dolabdjian K., Ströbele M., Romao C. P., Meyer H.-J. *Inorg. Chem*. 2019, *58*, 7845–7851.
27. Dolabdjian K., Meyer H.-J. *Z. Anorg. Allg. Chem*. 2017, *643*, 1898–1903.
28. Dutczak D., Ströbele M., Enseling D., Jüstel T., Meyer H.-J. *Eur. J. Inorg. Chem*. 2016, 4011–4016. https://doi.org/10.1002/ejic.201600118.
29. Dutczak D., Siai A., Ströbele M., Enseling D., Jüstel T., Meyer H. *Eur. J. Inorg. Chem*. 2020, 3954–3958. https://doi.org/10.1002/ejic.202000683.
30. Kallenbach P., Ströbele M., Meyer H. *Z. Anorg. Allg. Chem*. 2020, *646*, 1281–1284.
31. Hosono A., Stoffel R. P., Masubuchi Y., Dronskowski R., Kikkawa S. *Inorg. Chem*. 2019, *58*, 8938–8942.
32. Chen Z., Löber M., Rokicińska A., Ma Z., Chen J., Kuśtrowski P., Meyer H.-J., Dronskowski R., Slabon A. *Dalton Trans*. 2020, *49*, 3450–3456.
33. Corkett A. J., Chen K., Dronskowski R. *Eur. J. Inorg. Chem*. 2020, 2596–2602. https://doi.org/10.1002/ejic.202000244.
34. Qiao X., Mroz D., Corkett A. J., Bisswanger T., Dronskowski R. *Z. Anorg. Allg. Chem*. 2021, *647*, 496–499.
35. Braun C., Mereacre L., Hua W., Stürzer T., Ponomarev I., Kroll P., Slabon A., Chen Z., Damour Y., Rocquefelte X., Halet J.-F., Indris S. *ChemElectroChem* 2020, *7*, 4550–4561.
36. Riedel R., Greiner A., Miehe G., Dressler W., Fuess H., Bill J., Aldinger F. *Angew. Chem. Int. Ed*. 1997, *36*, 603–606.
37. Riedel R., Kroke E., Greiner A., Gabriel A. O., Ruwisch L., Nicolich J., Kroll P. *Chem. Mater*. 1998, *10*, 2964–2979.
38. Sougrati M. T., Darwiche A., Liu X., Mahmoud A., Hermann R. P., Jouen S., Monconduit L., Dronskowski R., Stievano L. *Angew. Chem. Int. Ed*. 2016, *55*, 5090–5095.
39. Liu X., Stork L., Speldrich M., Lueken H., Dronskowski R. *Chem. Eur J*. 2009, *15*, 1558–1561.
40. Franck H., Heimann H. Z. *Elektrochem. Angew. Phys. Chem*. 1927, *33*, 469–475.
41. Bredig M. A. *J. Am. Chem. Soc*. 1942, *64*, 1730–1731.
42. Vannerberg N.-G., Claeson G., Schotte L., Block-Bolten A., Toguri J. M., Flood H. *Acta Chem. Scand*. 1962, *16*, 2263–2266.

43. Hölsä J., Lamminmäki R.-J., Lastusaari M., Porcher P., Säilynoja E. *J. Alloys Compd.* 1998, *275–277*, 402–406.
44. Yuan S., Wang L., Xia B., Zhang H., Yang Y., Chen G. *Ceram. Int.* 2017, *43*, 16018–16022.
45. Yuan S., Wang L., Yang Y., Cheviré F., Tessier F., Chen G. *Ceram. Int.* 2016, *42*, 12508–12511.
46. Krings M., Montana G., Dronskowski R., Wickleder C. *Chem. Mater.* 2011, *23*, 1694–1699.
47. Reckeweg O., DiSalvo F. J. Z. *Anorg. Allg. Chem.* 2003, *629*, 177–179.
48. Wickleder C. *Chem. Mater.* 2005, *17*, 1228–1233.
49. Wickleder C. *J. Alloys Compd.* 2004, *374*, 10–13.
50. Pagano S., Montana G., Wickleder C., Schnick W. *Chem. Eur J.* 2009, *15*, 6186–6193.
51. Unverfehrt L., Ströbele M., Glaser J., Meyer H.-J. *Z. Anorg. Allg. Chem*. 2009, *635*, 1947–1952.
52. Sindlinger J., Glaser J., Bettentrup H., Jüstel T., Meyer H.-J. *Z. Anorg. Allg. Chem.* 2007, *633*, 1686–1690.
53. Eguía-Barrio A., Castillo-Martínez E., Liu X., Dronskowski R., Armand M., Rojo T. *J. Mater. Chem. A* 2016, *4*, 1608–1611.
54. Sougrati M. T., Arayamparambil J. J., Liu X., Mann M., Slabon A., Stievano L., Dronskowski R. *Dalton Trans*. 2018, *47*, 10827–10832.
55. Arayamparambil J. J., Mann M., Liu X., Alfredsson M., Dronskowski R., Stievano L., Sougrati M. T. *ACS Omega* 2019, *4*, 4339–4347.
56. Gibson K., Ströbele M., Blaschkowski B., Glaser J., Weisser M., Srinivasan R., Kolb H.-J., Meyer H.-J. Z. *Anorg. Allg. Chem.* 2003, *629*, 1863–1870.
57. Glaser J., Meyer H.-J. *Angew. Chem. Int. Ed.* 2008, *47*, 7547–7550.
58. Meyer H.-J. *Dalton Trans*. 2010, *39*, 5973–5982.
59. Qiao X., Ma Z., Luo D., Corkett A. J., Slabon A., Rokicinska A., Kuśtrowski P., Dronskowski R. *Dalton Trans*. 2020, *49*, 14061–14067.
60. Möller A., Konze P. M., Dronskowski R. Z. *Anorg. Allg. Chem*. 2018, *644*, 1881–1885.
61. Rodríguez-Carvajal J. FullProf(2k Version 4.40); Institut Laue-Langevin: Grenoble (France), 2008.
62. Adams K. M., Cooper M. J., Sole M. *J. Acta Crystallogr.* 1964, *17*, 1449–1451.
63. Bérar J. F., Lelann P. J. *Appl. Crystallogr.* 1991, *24*, 1–5.